PAPER

Check for updates

Intrafibrillar mineralization of type I collagen with calcium carbonate and strontium carbonate induced by polyelectrolyte–cation complexes†

Yizhou Zhang,‡[a] Yiru Wang,‡[a] Zhengyi Zhang,[a] Zhe Wang,[a] Changyu Shao, [ID][a] Matthias Hannig,[b] Zihuai Zhou [ID] *[a] and Baiping Fu [ID] *[a]

Calcium carbonate ($CaCO_3$), possessing excellent biocompatibility, bioactivity, osteoconductivity and superior biodegradability, may serve as an alternative to hydroxyapatite (HAp), the natural inorganic component of bone and dentin. Intrafibrillar mineralization of collagen with $CaCO_3$ was achieved through the polymer-induced liquid precursor (PILP) process for at least 2 days. This study aims to propose a novel pathway for rapid intrafibrillar mineralization with $CaCO_3$ by sequential application of the carbonate–bicarbonate buffer and polyaspartic acid (pAsp)-Ca suspension. Fourier transform infrared (FTIR) spectroscopy, zeta potential measurements, atomic force microscopy/Kelvin probe force microscopy (AFM/KPFM), and three-dimensional stochastic optical reconstruction microscopy (3D STORM) demonstrated that the carbonate–bicarbonate buffer significantly decreased the surface potential of collagen and CO_3^{2-}/HCO_3^- ions could attach to collagen fibrils *via* hydrogen bonds. The electropositive pAsp–Ca complexes and free Ca^{2+} ions are attracted to and interact with CO_3^{2-}/HCO_3^- ions through electrostatic attractions to form amorphous calcium carbonate that crystallizes gradually. Moreover, like $CaCO_3$, strontium carbonate ($SrCO_3$) can deposit inside the collagen fibrils through this pathway. The $CaCO_3$-mineralized collagen gels exhibited better biocompatibility and cell proliferation ability than $SrCO_3$. This study provides a feasible strategy for rapid collagen mineralization with $CaCO_3$ and $SrCO_3$, as well as elucidating the tissue engineering of $CaCO_3$-based biomineralized materials.

1 Introduction

Biominerals are formed in living organisms through self-regulation by incorporating natural elements into hierarchically structured organic–inorganic skeletons.[1] Biomineralization is a unique example of natural self-assembly and has arisen broad interests of scientists for decades.[2,3] The organic matrix typically serves as a template for biomineralization under the control of non-collagenous proteins (NCPs).[4] However, the inorganic minerals provide great mechanical and biological properties for the organic matrix.[5–7]

Carbonate minerals exist widely in the natural environment.[8] Among them, calcium carbonate ($CaCO_3$) is one of the most prevalent biominerals.[9] Aragonite, the metastable phase of

[a]*Stomatology Hospital, School of Stomatology, Zhejiang University School of Medicine, Zhejiang Provincial Clinical Research Center for Oral Diseases, Key Laboratory of Oral Biomedical Research of Zhejiang Province, Cancer Center of Zhejiang University, Engineering Research Center of Oral Biomaterials and Devices of Zhejiang Province, Hangzhou 310000. E-mail: fbp@zju.edu.cn; 11818406@zju.edu.cn*

[b]*Clinic of Operative Dentistry, Periodontology and Preventive Dentistry, Saarland University, 66421 Homburg, Germany*

‡ These authors contributed equally to this work.

$CaCO_3$, is the main inorganic phase of coral skeletons and nacre.[10,11] The skeletal parts of sea urchins, sea stars, and brittle stars are composed of calcite, the most stable phase of $CaCO_3$.[12] Herein, scientists have developed a large number of bio-inspired materials with $CaCO_3$ minerals making up the primary inorganic phase.[4]

Type I collagen is recognized as the most abundant fibrillar protein in the extracellular matrix and serves as a template for mineralization in hard tissues, including bone and dentin.[3,5] Hierarchical mineralization especially intrafibrillar mineralization endows the hard tissue with excellent mechanical and biological properties.[5–7] Hydroxyapatite (HAp) is the primary inorganic component of bone and dentin.[13] Replacement of intrafibrillar HAp crystallites with $CaCO_3$ might provide excellent biocompatibility, bioactivity, high osteoconductivity and superior biodegradability for the mineralized matrix.[3,14,15]

Intrafibrillar mineralization with $CaCO_3$ was previously achieved through the polymer-induced liquid precursor (PILP) process in various reconstituted collagen matrixes and demineralized natural dentin.[4,16–18] Intrafibrillar collagen mineralization with $CaCO_3$ was induced by amorphous calcium carbonate (ACC) precursors in the PILP process *via* capillary action or electrostatic attraction.[16,19,20] Nevertheless, despite the stability of polyelectrolytes, the supersaturated mineralizing media lost

their efficacy due to the crystallization of the metastable precursors in solution.[21] Moreover, the efficiency of the PILP process was significantly low, and mineralization was completed in at least two days.[18,22,23] Therefore, the clinical application and industrial production *via* the PILP process require further research and improvement.

NCPs play a crucial regulatory role in biomineralization due to their remarkable electronegativity. Anionic polyelectrolytes are widely used as NCP analogues.[4,19] The negatively charged polystyrene sulfonate (PSS) could capture numerous Ca^{2+} ions to form PSS–Ca complexes, attracting CO_3^{2-} ions to produce ACC for mineralization.[24] The PSS–Ca complexes immobilized onto Si_3N_4 substrates could interact with CO_3^{2-} ions through carbon dioxide (CO_2) gas diffusion, creating a local supersaturation that facilitates ACC formation.[25]

Following the discovery of polyelectrolyte–Ca complexes, we proposed the polyelectrolyte–calcium complex pre-precursor (PCCP) process for rapid collagen mineralization with HAp.[26] Mineralization was induced by using a highly concentrated polyaspartic acid (pAsp)-Ca suspension followed by a phosphate solution. However, intrafibrillar mineralization with $CaCO_3$ was not achieved using the pAsp-Ca suspension followed by the carbonate–bicarbonate buffer.

In contrast, intrafibrillar mineralization occurred when the application sequence was reversed in this study. The collagen fibrils were incubated in the carbonate–bicarbonate buffer for 3 h. CO_3^{2-}/HCO_3^- ions could infiltrate and bind to collagen *via* hydrogen bonds, significantly decreasing the surface potential of the collagen fibrils. After the treatment with the pAsp-Ca suspension for 30 min, the electropositive pAsp-Ca complexes and excess free Ca^{2+} ions were rapidly attracted to and interacted with CO_3^{2-}/HCO_3^- ions through electrostatic attraction. ACC formed inside the collagen and crystallized gradually (Fig. 1). The $CaCO_3$-mineralized collagen gels were biocompatible and promoted cell proliferation. Strontium is an indispensable element for the human body, resembling calcium in size and properties.[27,28] Herein, the calcium was replaced with strontium, and the intrafibrillar collagen mineralization with $SrCO_3$ was accomplished. This study provides a feasible strategy for intrafibrillar mineralization with $CaCO_3$ and $SrCO_3$ instead of the PILP and PCCP processes. It may highlight the potential biomedical applications of $CaCO_3$-based biomineralized materials.

2 Experimental

2.1. Materials and methods

The materials used in this study were commercially purchased. They included $NaHCO_3$, KCl, dimethyl sulphoxide (DMSO) and (3-aminopropyl) triethoxysilane (APTES) (Macklin Biochemical Co., China); hexamethyl disilylamine (HMDS), $SrCl_2\cdot6H_2O$, calcein sodium salt (Mw: 666.5 Da), 25 wt% of glutaraldehyde solution and phosphate buffered saline (PBS, 0.01 M, pH = 7.2–7.4) (Aladdin, China); poly-L-asparate acid (pAsp, Mw: 6–8 kDa, Aike Reagent, China); NaOH and Na_2CO_3 (Sinopharm Chemical Reagent Co., China); $CaCl_2\cdot2H_2O$, 5-fluorescein isothiocyanate, glycine, catalase, cysteamine and glucose oxidase (Sigma-Aldrich, USA); uranyl acetate (SPI-CHEM, USA); calcein/PI cell viability/cytotoxicity assay kit, blocking buffer and washing buffer (10×) (Beyotime, China); 300-mesh nickel TEM grids (Beijing XXBR Technology Co., China); Q-Sense gold-SiO_2 QCM wafer (Shenzhen Renlux Crystal Co., China); CCK-8 cell proliferation and cytotoxicity assay kit, penicillin-streptomycin liquid (100×), 0.25% of trypsin–EDTA solution and PBS (0.1 M, pH = 7.2–7.4) (Beijing Solarbio Science & Technology Co., China); fetal bovine serum (FBS, Biological Industries, Israel); bovine tendon type I collagen stock solution (Chengdu Kele Biological Technology Co., China); goat anti rabbit Alexafluor 647 antibody (ab150083) and rabbit anti-collagen I antibody (ab34710) (Abcam, UK); Dulbecco's modified eagle medium (DMEM, Hyclone, USA); type I collagen stock solution (rat tail, 3 mg mL^{-1}, Gibco-Invitrogen, USA).
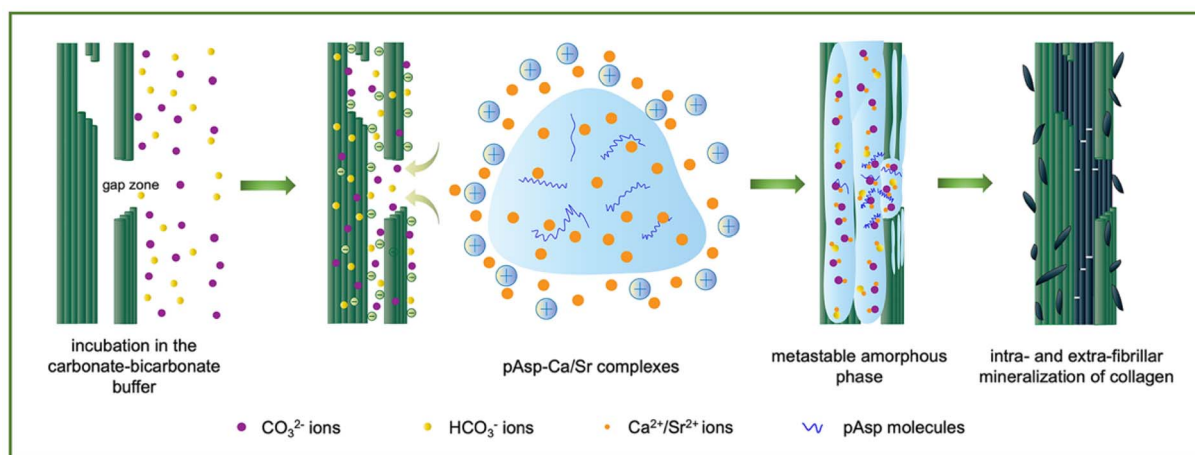

Fig. 1 Schematic diagram of the mineralization process proposed in this study. The CO_3^{2-}/HCO_3^- ions infiltrated and bound to collagen fibrils, followed by the recruitment of pAsp-Ca/Sr complexes and Ca^{2+}/Sr^{2+} ions. Intrafibrillar metastable amorphous mineral precursors were generated and eventually transformed into crystallites.

2.2. Preparation and characterization of the mineralizing media

2.2.1 Preparation of the carbonate–bicarbonate buffer and pAsp-Ca/Sr suspensions.

The carbonate–bicarbonate buffer was prepared by mixing 3.39 M sodium carbonate (Na_2CO_3) and 1.07 M sodium bicarbonate ($NaHCO_3$) solutions at a volume ratio of 1 : 3 and the pH value was exactly about 9.5 ± 0.2. The total concentration of CO_3^{2-} and HCO_3^{-} ions was approximately 1.65 M, resulting in a buffer concentration of 1.65 M. The pAsp-Ca suspension (4 g L^{-1}–5.44 M) was prepared by mixing 10 mL of 10 g L^{-1} pAsp solution and 20 g of $CaCl_2 \cdot 2H_2O$ and adjusting the pH to 9.5 ± 0.2 with 10 M NaOH. The final concentrations of pAsp and calcium were approximately 4 g L^{-1} and 5.44 M, respectively. Similarly, the pAsp-Sr suspension (2 g L^{-1} and 2.75 M) was prepared by dissolving 11 g of $SrCl_2 \cdot 6H_2O$ in 10 mL of 3 g L^{-1} pAsp solution and adjusting the pH to 9.5 ± 0.2 with 1 M NaOH. The final concentrations of pAsp and strontium were approximately 2 g L^{-1} and 2.75 M, respectively.

2.2.2 Characterizations of the pAsp-Ca/Sr complexes.

A 300-mesh nickel TEM grid was floated over 0.5 mL of the pAsp-Ca/Sr suspension for 30 s, rinsed with water and dried under lamp light. The grids were then analyzed with transmission scanning microscopy (TEM, JEM-1400, JEOL, Japan), scanning transmission electron microscopy with energy-dispersive X-ray spectroscopy (STEM-EDX, Nova Nano 450, Thermo FEI, USA) and high-resolution transmission scanning microscopy (HRTEM, JEM-2100F, JEOL, Japan) with selected area electron diffraction (SAED). The average diameters of the pAsp-Ca/Sr complexes were assessed using the Nano Measure1.2 software.

2.2.3 Measurements of the osmolarities of the pAsp-Ca/Sr suspensions.

The osmolarities of the pAsp-Ca/Sr suspensions were evaluated thrice with a freezing point osmometer (OM 806M, Löser Messtechnik, Germany). All suspensions were diluted 10 times before measurements due to the limited measurement range (0–2500 mOsm kg^{-1} H_2O) of the osmometer.

2.2.4 Measurements of the zeta potentials of the pAsp-Ca/Sr suspensions.

The zeta potentials of pAsp-Ca/Sr suspensions were measured at 633 nm using a Malvern Instrument Zetasizer (Nano ZS90, Malvern Instruments Ltd, UK).

2.3. Mineralization of the reconstituted single-layer type I collagen fibrils

2.3.1 Preparation of reconstituted single-layer type I collagen fibrils.

The reconstituted single-layer type I collagen fibrils were prepared as previously described.[29] Briefly, the collagen solution (50 mg L^{-1}) was obtained by mixing an 8.33 μL droplet of rat tail collagen stock solution with 0.5 mL of assembling solution (200 mM KCl, 50 mM glycine, pH = 9.2). The collagen solution was kept at room temperature for 20 min and dropped onto a 300-mesh nickel TEM grid, and incubated at 37 °C overnight. Afterwards, the reconstituted collagen fibrils were cross-linked in 0.05 wt% glutaraldehyde solution for 60 min and rinsed with deionized water. One grid was stained with 1% uranyl acetate and observed under a TEM to confirm the successful self-assembly of collagen fibrils.

2.3.2 Mineralization of single-layer type I collagen fibrils and characterizations.

The collagen-coated grids were suspended over 0.5 mL of the carbonate–bicarbonate buffer for 3 h at 37 °C and then blot-dried. The grids were then inverted and floated over either 1 mL of pAsp-Ca suspension for 30 min or pAsp-Sr suspension for 1 h at room temperature. The grids were gently rinsed with deionized water, and dehydrated in an ascending series of ethanol (50–100 v/v%). The mineralized collagen fibrils were finally evaluated with TEM, HRTEM with SAED, and STEM-EDX.

2.3.3 Three-dimensional stochastic optical reconstruction microscopy (3DSTORM) of the collagen fibrils mineralized with $CaCO_3$.

The STORM experiment was conducted to confirm the deposition of intrafibrillar $CaCO_3$ crystallites. The procedures were identical to those described in our previous study.[26] Briefly, the collagen fibrils were assembled on laser confocal culture dishes (LCCDs), which were first modified with APTES. The collagen fibrils were then stained immunofluorescently with rabbit anti-collagen I antibody and goat anti-rabbit Alexafluor 647 antibody. Calcein was used to label the Ca^{2+} ions in the pAsp-Ca suspension. Subsequently, the mineralized collagen fibrils were observed using a Nikon Ti-E inverted microscope (Nikon, Japan). The 3D-STORM images and videos were examined using Nikon NIS-Elements AR 4.51 software.

2.4. Mineralization of the reconstituted type I collagen gels

2.4.1 Preparation of the reconstituted type I collagen gels.

The reconstituted rat tail type I collagen gels were prepared as previously described.[30] The reconstituted collagen gels were obtained by mixing 300 μL of rat tail collagen stock solution with 75 μL of PBS buffer (0.1 M, pH = 7.2–7.4) and 50 μL of 0.1 N NaOH, followed by the incubation in a water bath at 30 °C for 3 days. Then, the gels were washed thrice with deionized water, cross-linked with 0.05 wt% glutaraldehyde for 2 h and immersed in deionized water for further experiments.

2.4.2 Mineralization of the reconstituted collagen gels.

The reconstituted collagen gels were divided into three distinct groups: pure collagen gels (CGs), $CaCO_3$-mineralized collagen gels (Ca-CGs) and $SrCO_3$-mineralized collagen gels (Sr-CGs). The collagen gels were initially immersed in the carbonate–bicarbonate buffer for 6 h and blot-dried for 3 min. The Ca-CGs were immersed in the pAsp-Ca suspension for 2 h, while the Sr-CGs were immersed in the pAsp-Sr suspension for 3 h, followed by thorough washing with deionized water.

2.4.3 Field emission scanning electron microscopy (FESEM) of the collagen gels.

The CGs, Ca-CGs, and Sr-CGs were dehydrated in an ascending series of ethanol (30–100 v/v%), ethanol-HMDS solution (50 v/v%) and HMDS, and eventually air-dried overnight. A gold layer was sputter-coated on the gels in an argon atmosphere with a sputter coater (K575X, Emitech, UK). The gels were then analyzed using an FESEM (SU8010, Hitachi, Japan) operating at an accelerating voltage of 3 kV for surface morphology observation.

2.4.4 Attenuated total reflectance-Fourier transform infrared (ATR-FTIR) spectra of the collagen gels.

The CGs, Ca-CGs, and Sr-CGs gels were dehydrated in an ascending series

of ethanol (30–100 v/v%) and air-dried. They were analyzed with ATR-FTIR (Nicolet iS10, Thermo Fisher Scientific, USA). The IR spectra were obtained at a resolution of 16 cm^{-1} from 400 to 4000 cm^{-1} with 100 scans each.

2.4.5 Powder X-ray diffraction (XRD) of the mineralized collagen gels. The Ca-CGs and Sr-CGs were lyophilized (Free Zone 2.5 Liter – 50C Benchtop Freeze Dryer, USA) for 1 day and crushed into powders. The XRD patterns of the powders (Gemini A Ohra, Oxford, UK) were obtained by using Ni-filtered Cu Kα radiation (20 mA, 30 KeV) in the 2θ range of 10–90°. The scan step time was 0.05 s, and the scan step size was 0.02 (2θ).

2.4.6 Thermogravimetric analysis (TGA) of the collagen gels. The CGs, Ca-CGs, and Sr-CGs were lyophilized for 1 day and crushed into powders for TGA (DSC1/400, TGA/DSC1 1100SF-MS, METTLER-TOLEDO, Switzerland). The analysis was carried out by increasing the temperature from 30 to 800 °C in a nitrogen atmosphere at a heating rate of 10 °C min^{-1}. Three specimens of each group were measured.

2.4.7 Inductively coupled plasma-atomic emission spectroscopy (ICP-OES) analysis of the mineralized collagen gels. The Ca-CGs and Sr-CGs were lyophilized and soaked in 10 mL of the PBS buffer (0.01 M, pH = 7.2–7.4). They were incubated at 37 °C for 28 days. The concentrations of Ca^{2+}/Sr^{2+} ions released in the PBS buffer were measured on days 1, 3, 5, 7, 14, 21 and 28 using ICP-OES (iCAP RQ ICP-MS, Thermo Fisher, USA). A total of 0.5 mL of immersion solution was retrieved and replaced with the fresh PBS buffer at each check time. The retrieved immersion solution was diluted to 10 mL with deionized water for ICP-OES analysis. All measurements were conducted in triplicate.

2.5. Biocompatibility testing

2.5.1 Cell culture. SD rat bone marrow mesenchymal stromal cells (rBMSCs) were commercially purchased (Cyagen Biosciences, Guangzhou, China). They were incubated in α-modified minimum essential medium (89% DMEM, 10% FBS and 1% (v/v) penicillin/streptomycin) under a 5% CO$_2$ atmosphere at 37 °C.

2.5.2 Cell proliferation. Cell proliferation on different collagen gels against rBMSCs was evaluated using the cell counting kit-8 (CCK-8). The CGs, Ca-CGs and Sr-CGs ($n = 3$) were disinfected by immersing in 75% ethanol 2 times for 5 min each. Subsequently, they were immersed in deionized water thrice for 10 min each to remove the ethanol and kept in the PBS buffer (0.01 M, pH = 7.2–7.4). Furthermore, they were incubated in 1 mL of culture medium for 30 min at 37 °C before use.[31] Finally, they were placed in 24-well plates, and 1×10^4 rBMSCs were seeded onto the samples in 1 mL of culture medium. After the co-cultivation for 1, 3, 5 and 7 days, the culture medium in each well was replaced with a mixing solution containing 90 μL of fresh medium and 10 μL of CCK-8 solution. The plates were subsequently incubated under 5% CO$_2$ at 37 °C for 3.5 h. The supernatant was retrieved and added to a 96-well plate. A microplate reader (Synergy H1, Bio-Tek, USA) was used to measure the optical density (OD) value.

2.5.3 Live/dead staining assay. The rBMSCs were seeded onto the CGs, Ca-CGs and Sr-CGs per the protocol outlined in Section 2.6.2. After the co-cultivation for 1, 3, 5 and 7 days, the samples were retrieved, rinsed with the PBS buffer (0.01 M, pH = 7.2–7.4) thrice and stained with calcein-AM/propidium iodide (PI) at each time point. Fluorescence images were captured using an inverted microscope (DMi 8, Leica, Germany).

2.6. The interaction of CO_3^{2-}/HCO_3^- ions with collagen fibrils

2.6.1 Fourier transform infrared (FTIR) spectra of the collagen gels. The reconstituted collagen gels were prepared following the protocol described in Section 2.4.1. The C-CGs (the experimental group) were treated with the carbonate–bicarbonate buffer for 3 h, while the control group (CG) was not. The CGs and C-CGs were then dehydrated and characterized using FTIR spectroscopy (Nicolet iS10, Thermo Fisher Scientific, USA). The infrared spectra were examined from 400–4000 cm^{-1} at a resolution of 4 cm^{-1} with 50 scans.

2.6.2 Circular dichroism (CD) spectra analysis of the collagen fibrils. CD spectra analysis was performed to identify the changes in the secondary structure of collagen (0.2 mg mL^{-1}) after a 3-hour incubation in the 15-fold diluted carbonate–bicarbonate buffer. A quartz cuvette with a path length of 1 mm was used. A spectropolarimeter (Chirascan V100, Applied Photophysics, UK) was employed to acquire CD spectra in the far-ultraviolet region (260–190 nm) with a scan speed of 100 nm min^{-1} at room temperature. Baseline correction was finished by subtracting the background of deionized water. Each spectrum represented an average of three scans.

2.6.3 Surface potential measurements of the collagen fibrils. Before and after the carbonate–bicarbonate buffer treatment, the surface potentials of collagen were examined to determine the effect of electrostatic attractions on the mineralization process. The protocols were similar to those proposed in our previous study.[26] Briefly, the collagen fibrils were assembled on gold-SiO$_2$ QCM wafers (5 MHz frequency, 0.3 mm thickness and 14 mm diameter). The assembled collagen fibrils were treated with the carbonate–bicarbonate buffer (serving as the experimental group) or not (serving as the control group). The surface potentials of collagen fibrils in both groups were measured with AFM/KPFM using nanoscale IR spectroscopy (NanoIR2, Anasys Instruments, USA). A KPFM tip (PR-EX-KPFM-5, Anasys, USA) coated with platinum–iridium with a nominal spring constant of 5 N m^{-1} was used. AFM measurements in peak force tapping mode were performed to detect the surface topography of the fibrils. KFPM measurements in tapping mode were conducted to measure the surface potentials of collagen fibrils. A contact potential difference (CPD) existed between the sample and tip. The tunable direct voltage compensated the CPD ($V_{CPD} = V_{tip} - V_{sample}$).[32] The V_{tip} value was determined by measuring the surface of a standard sample. A line was drawn in the center of collagen fibrils orienting with their long axis in topography and surface potential images for approximately 3215 nm using Analysis Studio v3.15 software (Anasys, USA) to obtain the surface potential and average potential values.

3 Results and discussion

3.1. Characterization of the pAsp-Ca/Sr suspensions

The pAsp-Ca/Sr suspension contained pAsp-Ca/Sr complexes and free Ca^{2+}/Sr^{2+} ions (Fig. 2).[26] Due to the limited solubility of $SrCl_2$, the concentration of the pAsp-Sr suspension was approximately half that of the pAsp-Ca suspension. One Ca^{2+} ion could bind to two carboxyl groups (–COOH) of one or two pAsp molecules.[26] Hence, the concentration of carboxyl groups from pAsp molecules in the pAsp-Ca suspension was calculated to be approximately 17.5 mM, which could capture 17.5–35.0 mM Ca^{2+} ions.[33] Similarly, approximately 8.75–17.5 mM Sr^{2+} ions could bind to pAsp molecules as the concentration of pAsp in the pAsp-Sr suspension was half that of the pAsp-Ca suspension. Due to the ultra-high Ca^{2+}/Sr^{2+} ion concentrations, numerous Ca^{2+}/Sr^{2+} ions were in the free ionic state in the suspension. The STEM images show that pAsp-Ca/Sr complexes were in irregular shapes (Fig. 2a and d). It could be ascribed to the random coil shapes of pAsp molecules.[34] The element mapping results reveal the distribution of calcium/strontium, carbon, oxygen, and nitrogen in the pAsp-Ca/Sr complexes (Fig. 2a and d). The HRTEM images with SAED patterns show the amorphous phase of these complexes (Fig. S1†). The average particle sizes of the pAsp-Ca and pAsp-Sr complexes were about 261.72 ± 12.42 nm and 298.69 ± 10.67 nm, respectively (Fig. 2b, c and e, f). Due to the abundance of Ca^{2+}/Sr^{2+} ions over the carboxyl groups, the zeta potentials of the pAsp-Ca and pAsp-Sr suspensions were 6.62 ± 0.18 and 6.99 ± 0.19 mV, respectively. Moreover, the osmolarities of the 10-time diluted pAsp-Ca and pAsp-Sr suspensions were 1303.67 ± 3.30 mOsm kg^{-1} and 669.33 ± 1.25 mOsm kg^{-1}, respectively, while those of the 10-time diluted pAsp solution were 2.00 ± 0.00 mOsm kg^{-1} and 1.00 ± 0.00 mOsm kg^{-1}, respectively. Therefore, the numerous Ca^{2+}/Sr^{2+} ions dominated the osmolarities, and pAsp molecules contributed minimally to the osmolarities of the pAsp-Ca/Sr suspensions.[26]

3.2. Intrafibrillar mineralization of reconstituted single-layer type I collagen fibrils

Reconstituted type I collagen stained with uranyl acetate exhibited typical periodic 67 nm patterns, indicating the successful self-assembly of collagen fibrils (Fig. S2†).[13] After the collagen fibrils were incubated in the carbonate–bicarbonate buffer for 3 h, no pronounced increase in the electron density of collagen fibrils was detected (Fig. 3a). The collagen fibrils were then treated with the pAsp-Ca suspension for 30 min, and both heavy intra- and extra-fibrillar mineralization were achieved (Fig. 3b and c). The HRTEM image (Fig. 3d) with SAED pattern (Fig. 3e) reveals that the intrafibrillar minerals were a mixture of vaterite and aragonite. The minor arc-shaped diffraction patterns suggest small lattice distortions between the boundaries of intrafibrillar crystallites (Fig. 3e). Aragonite (PDF 33-0268) is represented by (111), (002), and (041) planes, whereas the vaterite (PDF 41-1475) is represented by the (008) plane. The HRTEM image shows that the interplanar spacing of 3.40 Å is ascribed to the characteristic (111) crystal planes of aragonite (PDF 33-0268) (Fig. 3f). The STEM-EDX images exhibit the distribution of calcium, carbon, oxygen and nitrogen, indicating the deposition of $CaCO_3$ crystallites inside collagen fibrils (Fig. 3g).

Notably, the SAED pattern shows the multi-axial orientation of intrafibrillar $CaCO_3$ crystallites. The c-axis of intrafibrillar
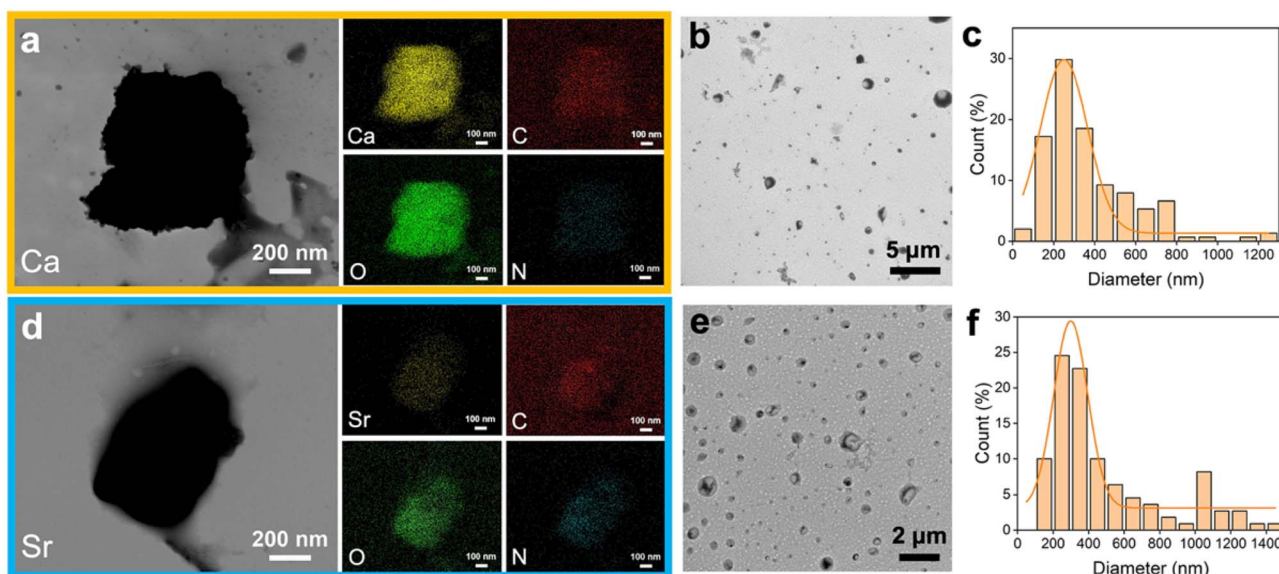

Fig. 2 Characterization of the pAsp–Ca/Sr complexes. (a) STEM image with elemental mapping results of an isolated pAsp–Ca complex. (b) TEM image of the pAsp–Ca complexes in the pAsp–Ca suspension. (c) The size distribution of the pAsp–Ca complexes in "b" reveals an average size of 261.72 ± 12.42 nm. (d) STEM image with elemental mapping results of an isolated pAsp–Sr complex. (e) TEM image of the pAsp–Sr complexes in the pAsp–Sr suspension. (f) The size distribution of the pAsp–Sr complexes in "e" reveals an average size of 298.69 ± 10.67 nm. Ca/Sr: yellow, C: red, O: green, N: blue.
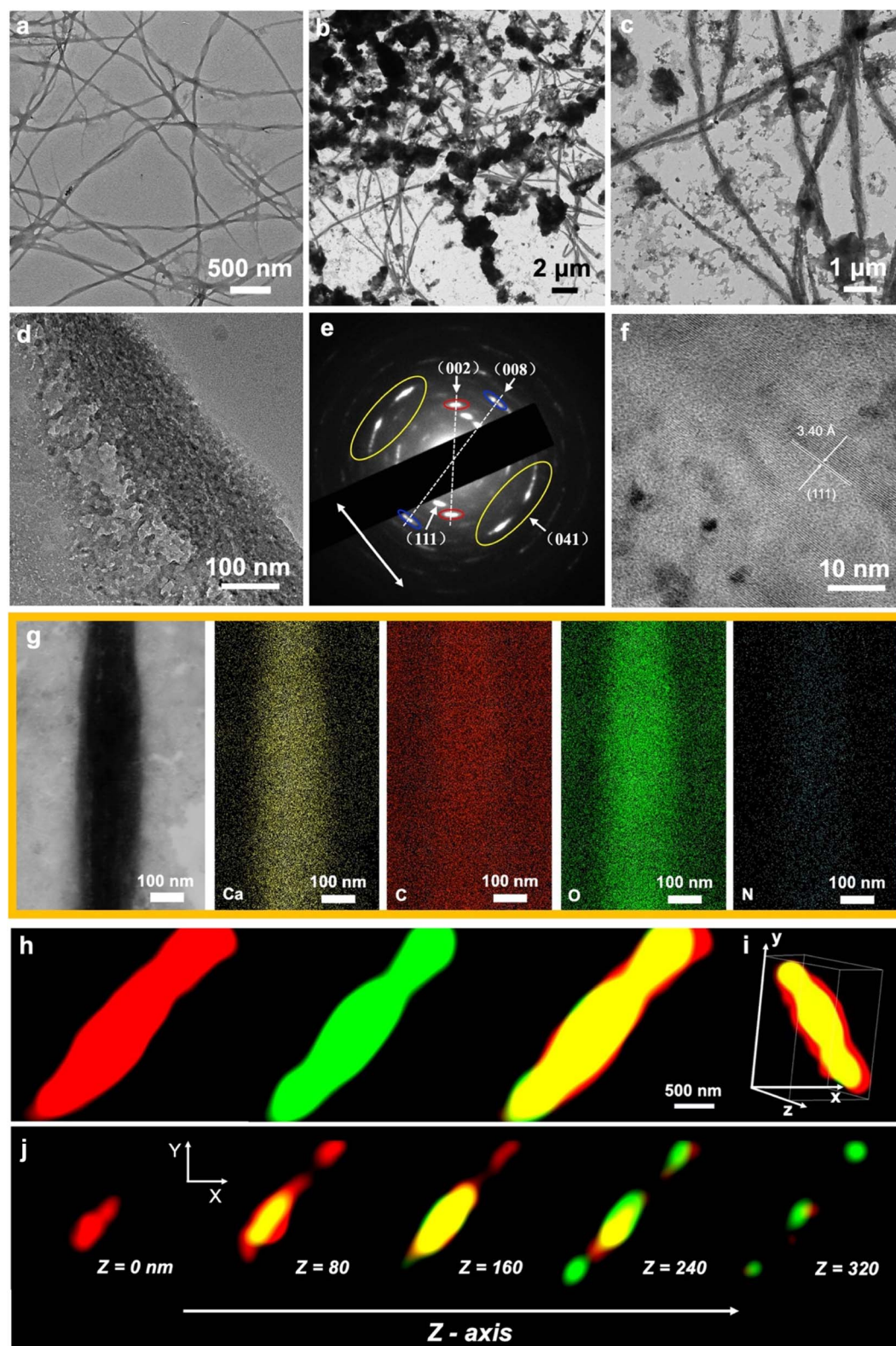
Fig. 3 Intrafibrillar mineralization of single-layer collagen fibrils with CaCO$_3$. (a) TEM image of the collagen fibrils incubated in the carbonate–bicarbonate buffer for 3 h. (b) TEM image of the mineralized collagen fibrils after the sequential incubation in the carbonate–bicarbonate buffer for 3 h and pAsp-Ca suspension for 30 min. (c) Magnification of "b". (d) HRTEM image of the mineralized collagen fibril. (e) SAED pattern of the collagen fibril in "d". The arcs of aragonite (002) diffraction, aragonite (041) diffraction and vaterite (008) diffraction are highlighted in red, yellow and blue circles, respectively. The long axis of the collagen fibril in "d" is highlighted with white arrows. (f) Magnification of the HRTEM image in "d". (g) STEM image with elemental mapping results of an isolated mineralized collagen fibril (Ca: yellow, C: red, O: green, N: blue). (h) The STORM images of a mineralized collagen fibril. The immunofluorescently labeled collagen fibril emitted red fluorescence. Calcein-labeled CaCO$_3$ emitted green fluorescence. Red fluorescence and green fluorescence were merged in yellow. (i) 3D visualization of the spatial distribution of intrafibrillar CaCO$_3$ crystallites. (j) The z-slices of the STORM images in "h" with an interval of 80 nm.

vaterite crystallites was nearly perpendicular to the collagen long axis, while the intrafibrillar aragonite crystallites were oriented with the (041) crystal plane along the fibril (Fig. 3e). Vaterite and aragonite phases have anisotropic crystal structures, however, they prefer to grow along their c-axis.[23,35] This may indicate that ACC initially filled gap zones, transformed into vaterite crystallites and deposited inside the gap zones. Intrafibrillar vaterite crystallites grew along their c-axis approximately perpendicular to the collagen long axis due to the confinement within gap zone channels.[23] The residual ACC occupied the overlap zones and transformed into aragonite phase.[23] However, the intrafibrillar aragonite crystallites were oriented with the (041) crystal plane along the fibril rather than their c-axis. It could be due to the polycrystalline structures inside the fibrils. The differences in crystal morphologies between vaterite and aragonite and the confinement induced by the collagen may change the fastest-growing direction and distort the structure of aragonite crystallites.

The intrafibrillar mineralization with $CaCO_3$ was further verified *via* the STORM technique. The immunofluorescently labelled collagen fibrils emitted red fluorescence and calcein-labelled $CaCO_3$ crystallites emitted green fluorescence (Fig. 3g). The overlapping yellow regions in 3D visualization (Fig. 3h) and continuous z-slicing of the reconstructed 3D-STORM model (Fig. 3i) represent the intrafibrillar $CaCO_3$ crystallites.

To validate the efficacy of the proposed pathway, the pAsp-Sr suspension was applied in the same way (Fig. 4). The TEM images exhibit heavy intra- and extra-fibrillar mineralization of collagen fibrils after the incubation in the carbonate–bicarbonate buffer for 3 h followed by the pAsp-Sr suspension for 1 h (Fig. 4a and b). The HRTEM image with the SAED pattern reveals typical (111), (002), (012), (200), (221) and (132) planes of the intrafibrillar $SrCO_3$ crystallites (PDF 05-0418) (Fig. 4c). Furthermore, the typical diffraction arc (002) indicates that intrafibrillar $SrCO_3$ crystallites grew along their c-axis, parallel
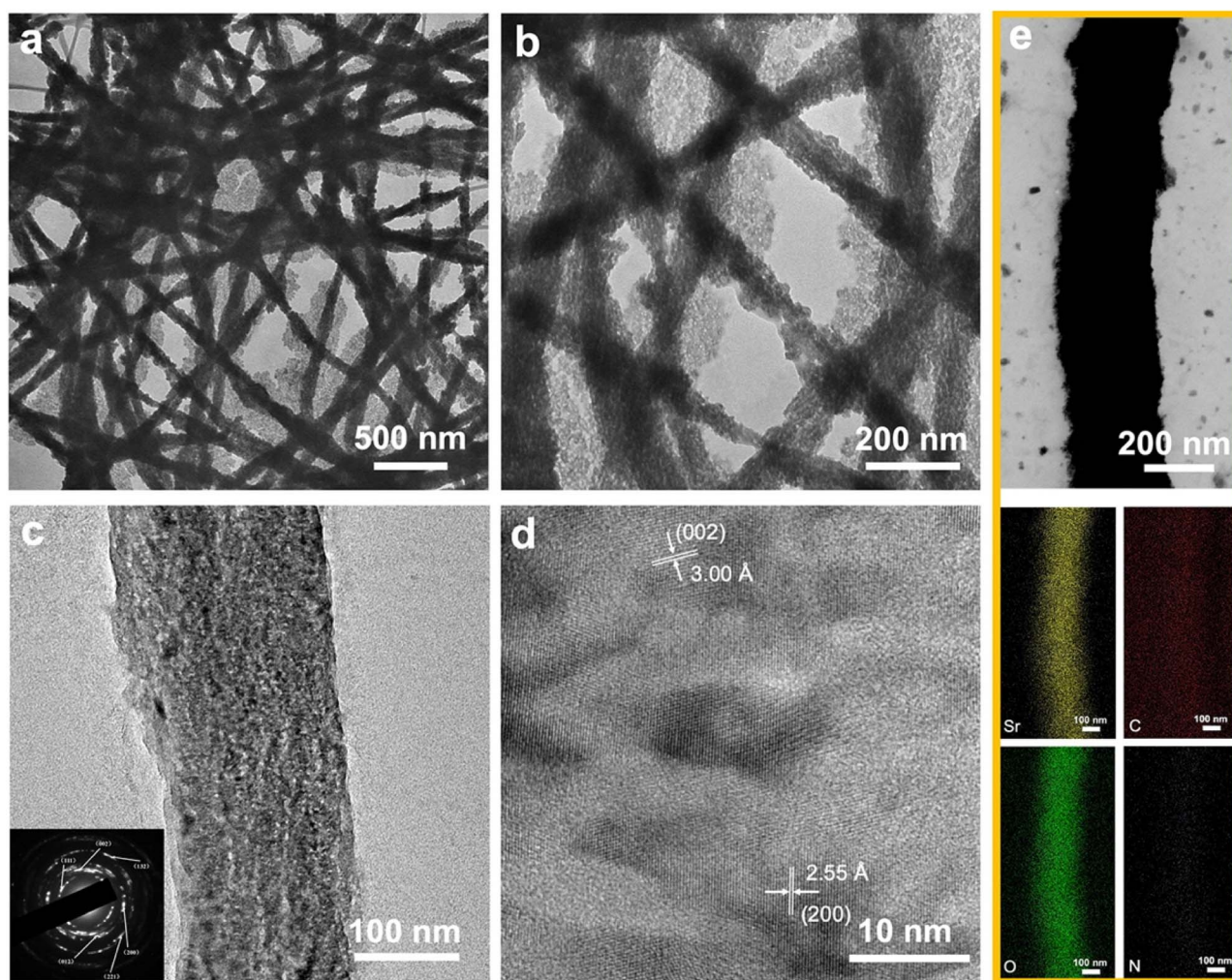

Fig. 4 Intrafibrillar mineralization of single-layer collagen fibrils with $SrCO_3$. (a) TEM image of the mineralized collagen fibrils after sequential incubation in the carbonate–bicarbonate buffer for 3 h and pAsp-Sr suspension for 1 h. (b) Magnification of "a". (c) HRTEM image with the SAED pattern of a mineralized collagen fibril. (d) Magnification of the HRTEM image in "c". (e) STEM image with elemental mapping results of a mineralized collagen fibril (Sr: yellow, C: red, O: green, N: blue).

to the long axis of the fibril. The HRTEM image shows that the interplanar spacings of 2.55 Å and 3.00 Å correspond to the characteristic (200) and (002) crystal planes of $SrCO_3$, respectively (PDF 05-0418) (Fig. 4d). The STEM image of the mineralized collagen fibril exhibits a high electron density, and elemental mapping images show the distributions of strontium, carbon, oxygen and nitrogen, indicating the deposition of $SrCO_3$ crystallites within fibrils (Fig. 4e).
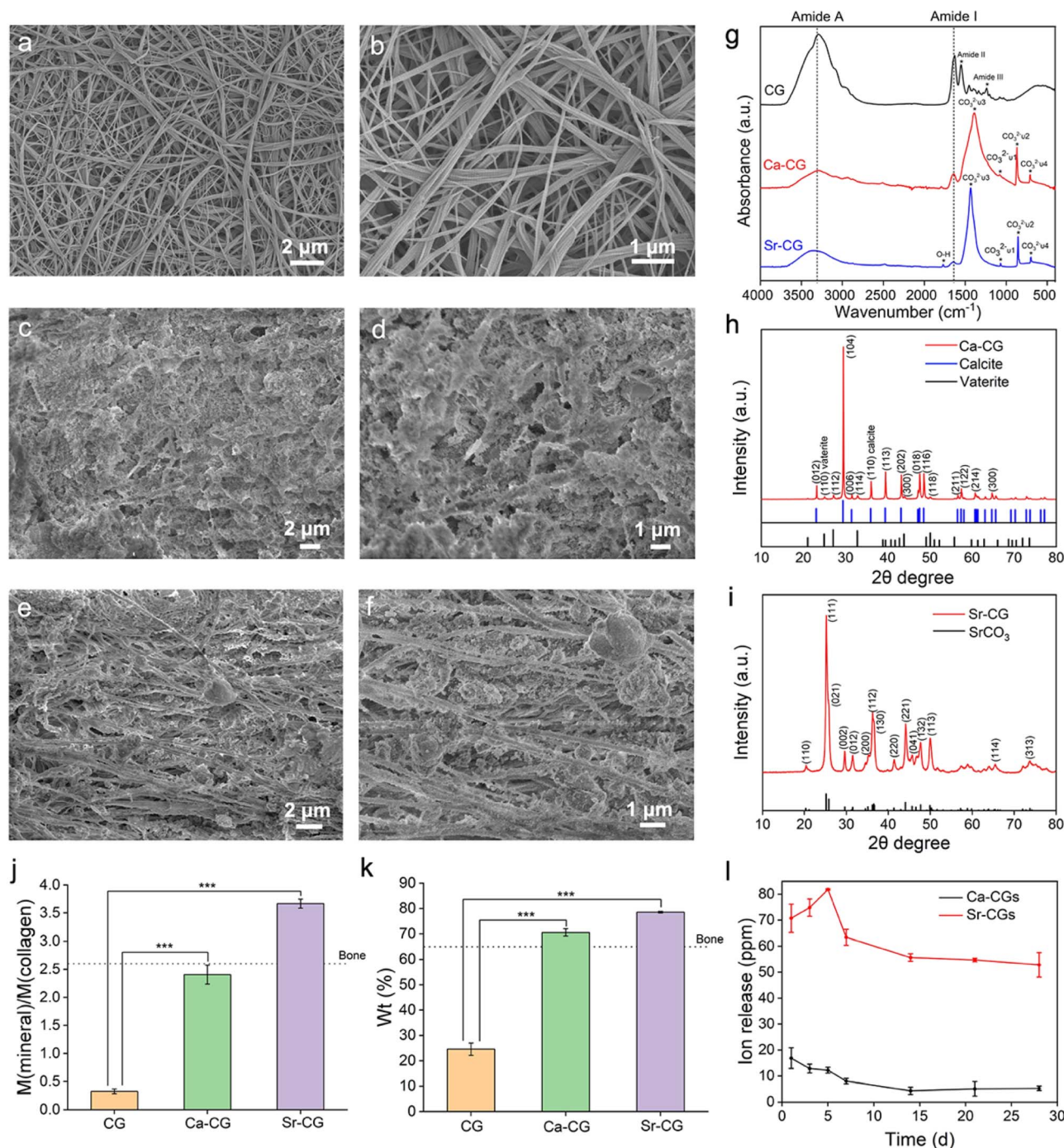

Fig. 5 Characterization of the CGs, Ca-CGs and Sr-CGs. (a–f) FESEM images of the unmineralized/mineralized reconstituted collagen gels. (a and b) Low- (a) and high- (b) magnification images of the CG reveal a smooth surface of the pure collagen fibrils. (c and d) Low- (c) and high (d) magnification images of the Ca-CG show a rough surface of the collagen fibrils. (e and f) Low- (e) and high- (f) magnification images of the Sr-CG indicate heavy mineralization. (g) ATR-FTIR spectra show the typical absorption peaks of CO_3^{2-} ions in Ca-CG and Sr-CG in comparison with CG. (h and i) XRD spectra of the Ca-CG (h) and Sr-CG (i) confirm the existence of $CaCO_3$ and $SrCO_3$ crystallites inside the collagen gels, respectively. (j and k) TGA results of CGs, Ca-CGs and Sr-CGs. The calculated mineral/collagen weight ratios (j) and mineral weight percentages (k) show that the mineral contents of Ca-CGs and Sr-CGs were significantly higher than those of CGs ($n = 3$, ***$P < 0.001$). (l) The Ca^{2+}/Sr^{2+} ion release curves of Ca-CGs and Sr-CGs show a sustained release of Ca^{2+} ions during 28 days and a burst release of Sr^{2+} ions during the first 5 days.

3.3. Mineralization of the reconstituted type I collagen gels (CGs)

The reconstituted single-layer collagen model is two-dimensional (2D), whereas the natural collagen matrix in hard tissues is three-dimensional (3D) and difficult to mineralize.[36] Therefore, the reconstituted type I collagen gel was used as a 3D collagen model to validate the proposed process. The pure collagen gel exhibited a smooth surface with a typical D-band pattern (Fig. 5a and b). The collagen fibrils of the mineralized gels were embedded in the minerals, and the structure was unclear (Fig. 5c–f). The Ca-CG contained massive crystals resembling the typical rhombohedral calcite structure (Fig. 5c and d) in the interfibrillar spaces.[37] The loosely formed interfibrillar spherical crystals could be observed in the Sr-CG (Fig. 5e and f).

The ATR-FTIR spectra and XRD patterns were used to identify the minerals within the collagen gels. The ATR-FTIR spectrum of the CG shows the characteristic peaks of amide I (C=O stretch), amide II (N–H in-plane bend), amide III (C–N stretch and the N–H in-plane bend) and amide A (N–H stretch) bands at 1630 cm^{-1}, 1552 cm^{-1}, 1241 cm^{-1} and 3293 cm^{-1}, respectively (Fig. 5g).[38] The characteristic peaks of 1391 cm^{-1}, 1082 cm^{-1}, 871 cm^{-1} and 711 cm^{-1} of the Ca-CG are assigned to the $\nu 3$, $\nu 1$, $\nu 2$ and $\nu 4$ absorption bands of CO_3^{2-} ions, respectively. The CO_3^{2-} $\nu 2$ and $\nu 4$ bands indicate the presence of vaterite and calcite, respectively.[18,39] The presence of calcite is consistent with the rhombohedral particles in the interfibrillar space (Fig. 5c and d).[4] As for the Sr-CG, the characteristic peak at 1771 cm^{-1} corresponds to the O–H vibration, while the peaks at 1436 cm^{-1}, 1071 cm^{-1}, 856 cm^{-1} and 705 cm^{-1} correspond to the $\nu 3$, $\nu 1$, $\nu 2$ and $\nu 4$ vibrations bands of CO_3^{2-} ions, respectively (Fig. 5g).[40] The XRD patterns are consistent with the ATR-FTIR spectra. The XRD pattern of the Ca-CG reveals that the diffraction peaks correspond to the (012), (104), (006), (110), (113), (202), (018), (116), (211), (122), (214) and (300) crystal planes of the calcite phase (PDF 47-1743) and the (110), (112), (114), (300) and (118) crystal planes of the vaterite phase (PDF 33-0268) (Fig. 5h). Compared with the SAED result (Fig. 3e) of the single-layer collagen model, no aragonite was detected in the collagen gels. The intrafibrillar aragonite might transform into the calcite phase in the collagen gel model. The XRD pattern of the Sr-CG shows distinct diffraction peaks, including (110), (111), (021), (002), (012), (200), (112), (130), (220), (221), (041), (132), (113), (114) and (313) crystal planes of the $SrCO_3$ phase (PDF 05-0418) (Fig. 5i), corroborating the deposition of $SrCO_3$ crystallites in the Sr-CG.

The weight ratio of mineral/collagen and the weight percentage of minerals inside the gels were estimated based on the TGA results. The weight loss below 200 °C was ascribed to the evaporation of water. The weight loss between 200 and 600 °C was assigned to the decomposition of collagen.[29] The residual weight represented inorganic minerals, because the decomposition temperatures of $CaCO_3$ and $SrCO_3$ crystallites are both higher than 600 °C.[41–45] As a consequence, the mineral/collagen weight ratios of Ca-CGs and Sr-CGs were 2.40 ± 0.137 and 3.67 ± 0.065, respectively, evidently higher than CGs (0.327

± 0.034, $P < 0.001$) (Fig. 5j). The weight percentages of Ca-CGs and Sr-CGs were $70.58 \pm 1.18\%$ and $78.57 \pm 0.30\%$, respectively, markedly higher than $24.58 \pm 1.98\%$ of CGs ($P < 0.001$) (Fig. 5k). The mineral content of the mineralized collagen gels was comparable to that of natural bone, which contains 65 wt% mineral phase.[13,46] The calculated atomic contents of calcium and strontium per gram of pure collagen gel were 24.21 ± 1.39 mM and 24.84 ± 0.44 mM, respectively. Therefore, the concentrations of $CaCO_3$ and $SrCO_3$ per unit mass of the pure collagen gel were similar ($P > 0.05$).

ICP-OES measurements determined the ion release of Ca-CGs and Sr-CGs. The ion release curve indicates a sustained release of Ca^{2+}/Sr^{2+} ions during 28 days. The concentration of Ca^{2+} ions was 16.87 ± 4.00 ppm on day 1, gradually decreasing to 4.32 ± 1.40 ppm on day 14, thus maintaining stability. However, the Sr^{2+} ion release curve exhibits a burst release of Sr^{2+} ions in the initial stage, increasing from 70.73 ± 4.42 ppm on day 1 to 81.82 ± 0.36 ppm on day 5. Afterwards, the release of Sr^{2+} ions dropped sharply to a plateau of 63.43 ± 3.74 ppm on day 14 (Fig. 5l). The concentration of Sr^{2+} ions released substantially surpassed that of Ca^{2+} ions at each time point ($P < 0.001$), despite the equality in $CaCO_3$ and $SrCO_3$ concentrations per unit mass within the pure collagen gel (Fig. 5k). Moreover, $CaCO_3$ presents a higher solubility compared to $SrCO_3$.[47,48] It might imply a higher degree of intrafibrillar mineralization of Ca-CGs than Sr-CGs, as the collagen could be a predictable barrier to prevent the outflow of functional cations, and the intrafibrillarly mineralized collagen gels are predisposed to release cations sustainably.[49] Moreover, the higher crystallinity of intrafibrillar minerals inside Ca-CGs *versus* Sr-CGs might result in better retention of intrafibrillar $CaCO_3$ crystallites.

3.4. Evaluation of the biocompatibility of mineralized collagen gels

The collagen gel model could be used to mimic the physiological extracellular organic matrix for evaluation of the biocompatibility of mineralized collagen materials.[50] Numerous studies indicate that calcium and strontium promote bone formation in adequate concentrations,[51–53] therefore, we attempted to incorporate Ca^{2+}/Sr^{2+} ions into the reconstituted collagen gels *via* biomimetic mineralization. Hence, the biocompatibility of Ca-CGs and Sr-CGs as potential biomedical materials was assessed by CCK-8 assay and live/dead staining assay. According to the results of CCK-8 assay, CGs, Ca-CGs and Sr-CGs exhibited comparable levels of cell proliferation after 1 day of co-cultivation with rBMSCs. The cell proliferation on Ca-CGs was remarkably higher than CGs on days 3 and 7, and higher than Sr-CGs on days 3, 5 and 7, suggesting their superior biocompatibility and noncytotoxicity. However, the cell proliferation on Sr-CGs showed insignificant differences compared to CGs during the first 3 days and even a lower level on days 5 and 7, suggesting cell cytotoxicity of Sr-CGs (Fig. 6a). The live/dead staining assay also revealed comparable results (Fig. 6b). No significant dead cells (red staining) were found in CGs and Ca-CGs during the 7-day cultivation. The cells in both groups demonstrated satisfactory cell proliferation, indicating the

biocompatibility of CGs and Ca-CGs. Furthermore, the cells on Ca-CGs proliferated faster than cells on CGs and Sr-CGs at each time point, implying that $CaCO_3$ could stimulate cell proliferation. However, compared to CGs, more dead cells were found in Sr-CGs after 3-day cultivation and the cell proliferation rate

was apparently slower on days 5 and 7, implying cell cytotoxicity of Sr-CGs. The results abovementioned were consistent with the release curve of Sr^{2+} ions, which showed a burst release in the first 5 days and the concentration of Sr^{2+} ions was significantly higher than Ca^{2+} ions all the time ($P < 0.001$) (Fig. 5l), because
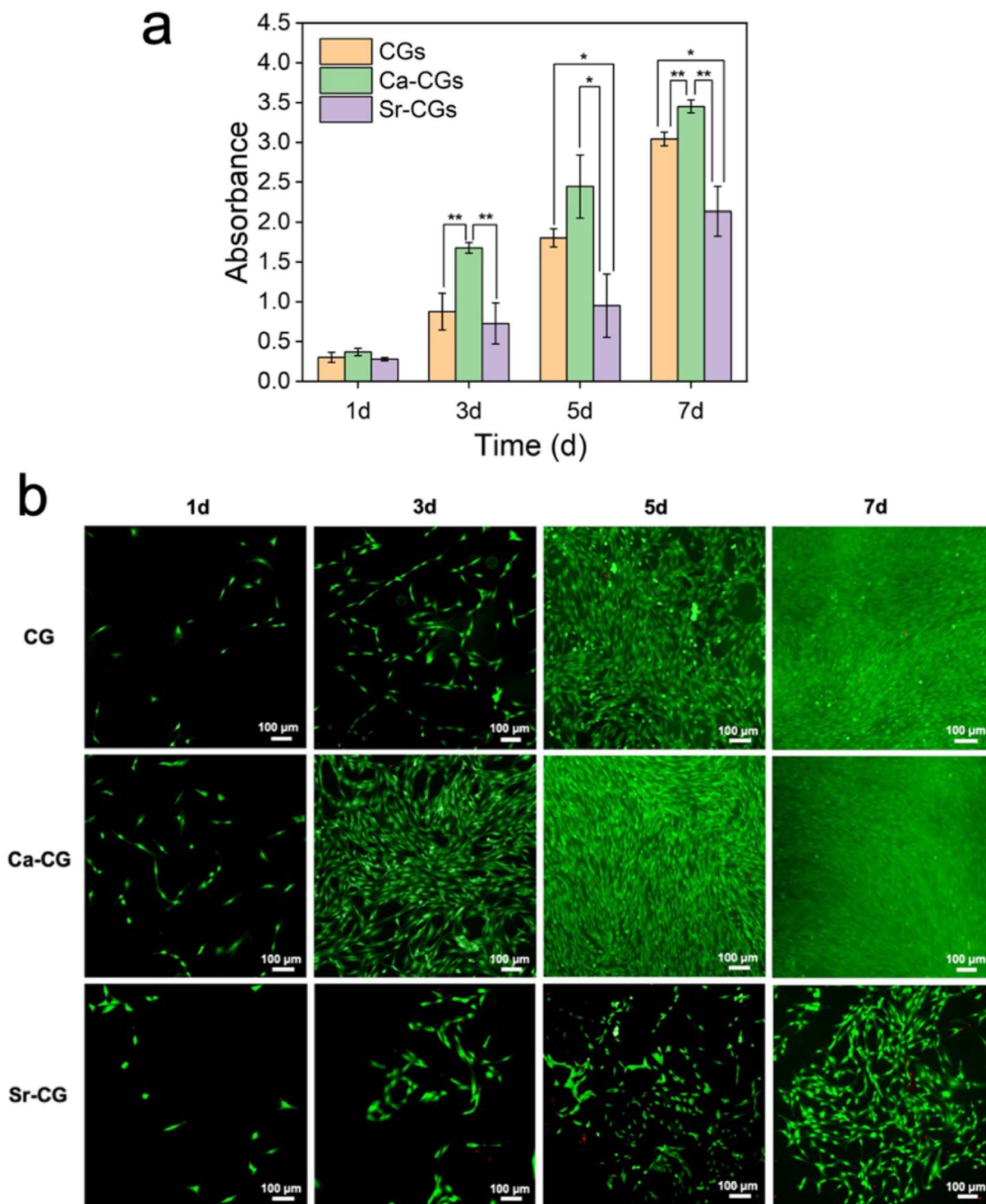

Fig. 6 Biocompatibility of mineralized collagen gels against rBMSCs. (a) CCK-8 assay results of CGs, Ca-CGs and Sr-CGs co-cultivated with rBMSCs for 1, 3, 5 and 7 days ($n = 3$, *$P < 0.05$, **$P < 0.01$). (b) Fluorescence microscopic images of rBMSCs co-cultured with CGs, Ca-CGs and Sr-CGs for 1, 3, 5 and 7 days using calcein-AM/PI staining. Live and dead cells were stained in green and red, respectively.

a high dose of Sr^{2+} ions could induce cell cytotoxicity on rBMSCs.[54] Similar results have been reported for pure strontium HAp (without calcium in the HAp) as a high concentration of the released Sr^{2+} ions caused cytotoxicity and limited its application in hard tissue regeneration.[30]

Overall, Ca-CGs are more compatible with rBMSCs than Sr-CGs. However, their potential to promote osteogenesis and the associated pathway still requires further research. Intrafibrillar mineralization with Sr-doped $CaCO_3$ could potentially yield osteopromotive effects as the strontium element has been amply documented for its capacity to stimulate osteogenesis.[27] We have recently attempted (Fig. S3–S5†) and achieved (Fig. S5†) intrafibrillar mineralization with Sr-doped $CaCO_3$ using reconstituted single-layer collagen models. Further research is required to explore its application potential in biomedical fields.

3.5. Differences between the proposed process and the PILP and PCCP processes

Calcium phosphate (CaP) is the main inorganic component of natural bone and dentin.[3] $CaCO_3$ might be an alternative to HAp due to its high bioactivity, biocompatibility, high osteoconductivity and superior biodegradability compared to HAp.[3,14,15] $CaCO_3$-based collagen materials with intrafibrillar $CaCO_3$ crystallites deposition could be recognized as a blueprint for hard tissue regeneration.[14,55,56] Until now, intrafibrillar mineralization with either CaP or $CaCO_3$ has been achieved *via* the PILP process.[16,19,57] The PILP process is based on liquid-like amorphous mineral precursors with plasticity and high hydration that infiltrate collagen fibrils through gap zones.[20,58] NCPs or their analogs could initially inhibit nucleation and stabilize the formed ACC phase.[4] The ACC penetrated into the collagen fibrils probably through capillary action or electrostatic attraction.[16,19,20] The clinical and industrial applications of the PILP process are restricted by the limited mineralization efficiency at such low concentrations and the instability of ACC precursors.

To overcome these limitations, the polyelectrolyte–calcium complex pre-precursor (PCCP) process was proposed to induce rapid intrafibrillar mineralization for reconstituted collagen fibrils and demineralized dentin matrix by sequentially applying ultra-highly concentrated pAsp-Ca suspension and phosphate solution.[26,59] Amorphous calcium phosphate (ACP) was generated inside the collagen fibrils and gradually transformed into HAp in artificial saliva. Moreover, intrafibrillar mineralization could not be achieved when the sequences of the pAsp-Ca suspension and phosphate solution order were switched.[26] The electronegative phosphate groups were excluded from the collagen fibrils due to the electrostatic repulsion. Extrafibrillar apatite deposition was observed even after the fibrils were treated with the pAsp-Ca suspension. Similar procedures were used for intrafibrillar mineralization with $CaCO_3$ to discover a new pathway for manufacturing $CaCO_3$-based biomineralized materials. However, the anticipated intrafibrillar mineralization could not be achieved when the fibrils were sequentially treated with the pAsp-Ca suspension and carbonate–bicarbonate buffer (Fig. S6†). ACC was initially generated within collagen fibrils, while intrafibrillar minerals gradually decreased in the carbonate–bicarbonate buffer (Fig. S6†). This phenomenon could be explained by the experiment demonstrating that ACC could be intrinsically stabilized by HCO_3^- ions in a physiological environment.[60] Herein, intrafibrillar ACC was stabilized by numerous HCO_3^- ions in the carbonate–bicarbonate buffer and gradually diffused outwards. Intrafibrillar mineralization occurred when the collagen fibrils were treated with the carbonate–bicarbonate buffer before pAsp-Ca suspension (Fig. 3).

To better understand the mechanism of the proposed strategy in this study, the interaction between CO_3^{2-}/HCO_3^- ions and collagen fibrils was further explored *via* FTIR spectra, CD spectra and AFM/KPFM analyses. The FTIR spectrum of the carbonate–bicarbonate buffer-treated collagen gel (C-CG) shows a decreased intensity of the characteristic peaks of collagen (1652 cm^{-1}, 1554 cm^{-1}, 1239 cm^{-1} and 3318 cm^{-1}) compared to CGs. The new peaks at 866 cm^{-1}, 1083 cm^{-1} and 1453 cm^{-1} represent the $\nu2$, $\nu1$ and $\nu3$ vibrational modes of the CO_3^{2-}/HCO_3^- ions, respectively. The peak at 1033 cm^{-1} is assigned to the C–OH group of HCO_3^- ions.[61] The peak of amide A (N–H stretching vibration) slightly redshifts from 3328 cm^{-1} to 3318 cm^{-1} due to the hydrogen bond between CO_3^{2-}/HCO_3^- ions and collagen, stabilizing the triple-helical structure of collagen (Fig. 7a).[62,63]

Additionally, CD spectra analysis was used to analyze the changes in the secondary structure of collagen.[64] In the CD spectra, a minimum negative absorption peak at 197 nm, and a crossover point at 214 nm along with a maximal positive absorption peak at 222 nm reveal the triple helical conformation characteristics of both pure collagen and the carbonate–bicarbonate buffer-treated collagen.[65] The parameter Rpn, the ratio of the absolute peak intensities at 222 nm and 197 nm, is a criterion for evaluating the triple helical conformation of collagen.[66] In our experiment, the Rpn values of pure collagen and the carbonate–bicarbonate buffer-treated collagen were measured to be 0.1180 and 0.1311, respectively (Fig. 7b), indicating a higher stability of the collagen triple helix after the incubation in the carbonate–bicarbonate buffer.[63] This result was consistent with the FTIR spectra of the hydrogen bond formed between collagen fibrils and CO_3^{2-}/HCO_3^- ions (Fig. 7a).

AFM/KPFM was used to identify changes in the surface potential of the collagen fibrils after the incubation in the carbonate–bicarbonate buffer (Fig. 7c–h). The AFM image shows the typical periodic banding structure of the pure assembled collagen (Fig. 7c). The surface potentials along the collagen fibril exhibited interlaced positive and negative peaks with an average surface potential value of -0.83 ± 1.50 mV (Fig. 7d and e). No apparent topographical changes were observed in the collagen fibrils after a 3-hour incubation in the carbonate–bicarbonate buffer (Fig. 7f). The treated collagen fibrils were negatively charged with an average surface potential value decreasing to -29.07 ± 5.69 mV ($P < 0.001$) (Fig. 7g and h).

The spatial distribution of pAsp molecules was also investigated *via* the 3D-STORM technique. The pAsp molecules were found to be inside the carbonate–bicarbonate treated fibrils after the incubation in pAsp-Ca suspension for 30 min
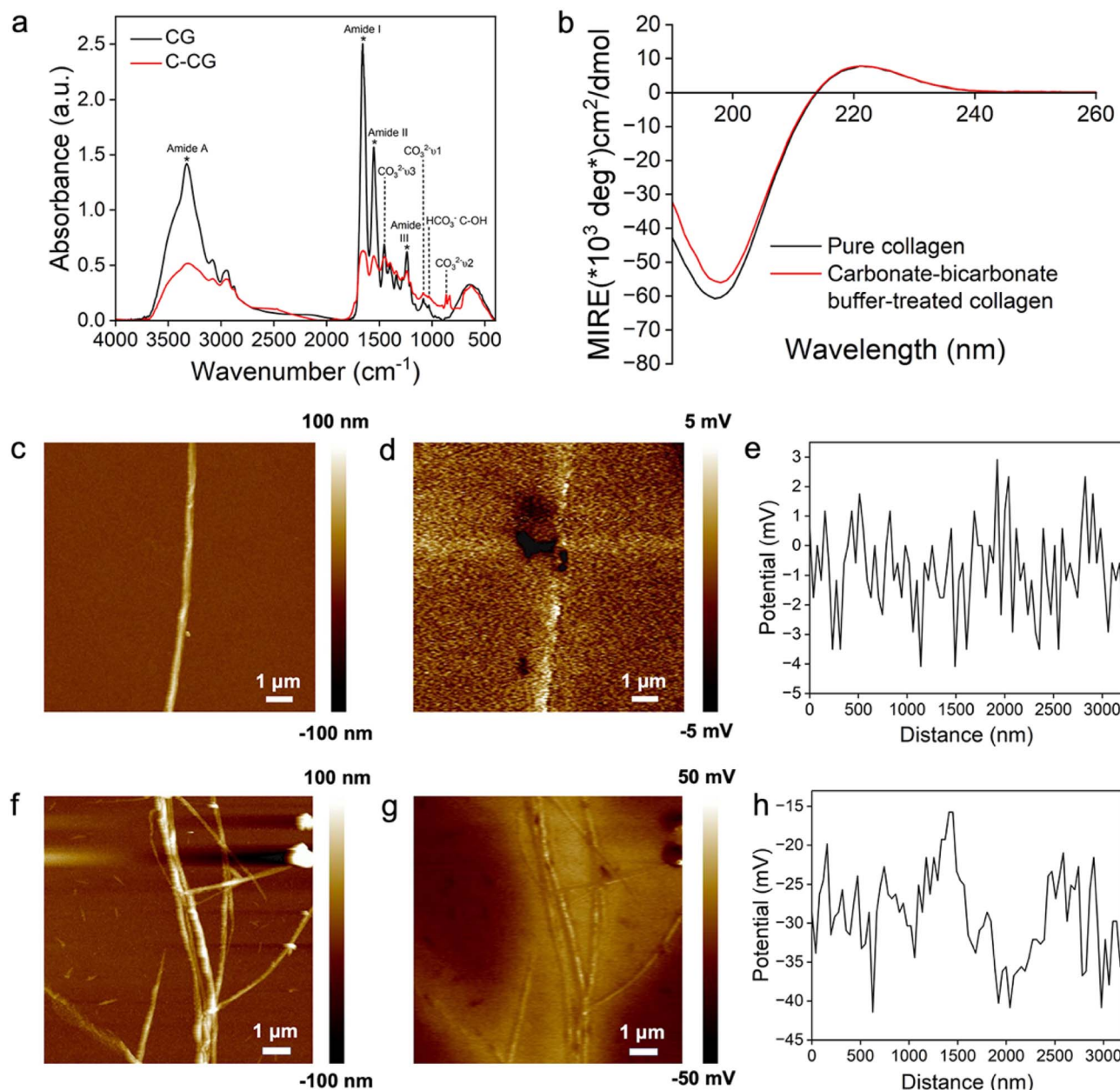
Fig. 7 The influence of CO_3^{2-}/HCO_3^- ions on the structure of collagen fibrils. (a) FTIR spectra of the CG and C-CG. (b) CD spectra of the pure collagen and carbonate–bicarbonate buffer-treated collagen. (c–h) AFM/KPFM images and surface potentials of pure collagen (c–e) and carbonate–bicarbonate buffer treated-collagen (f–h). The topography (c) and V_{CPD} distribution (d) of the pure collagen fibril were measured to calculate the surface potential distribution ($V_{sample} = V_{tip} - V_{CPD}$) along the collagen fibril, revealing an average surface potential of -0.83 ± 1.50 mV (e). The topography (f) and V_{CPD} distribution (g) of the carbonate–bicarbonate buffer-treated collagen fibril were analyzed to calculate the average surface potential as -29.07 ± 5.69 mV (h).

(Fig. S7†). In corroboration with the findings indicating that Ca^{2+} ions were also inside the fibrils (Fig. 3h–j), it could be concluded that pAsp-Ca complexes infiltrated the carbonate–bicarbonate treated-collagen fibrils after 30 min-incubation in the pAsp-Ca suspension.

4 Conclusion

In contrast to the PILP and PCCP processes, the CO_3^{2-}/HCO_3^- ions could interact with and attach to the collagen fibrils *via* hydrogen bonds, improving the stability of the collagen triple-helix structure and increasing the electronegativity of collagen fibrils, that facilitate the infiltration of pAsp-Ca/Sr complexes and Ca^{2+}/Sr^{2+} ions through electrostatic attraction. Subsequently, ACC/ASC formed and crystallized gradually within collagen, inducing intrafibrillar mineralization with $CaCO_3/SrCO_3$. The acquired Ca-CGs had better biocompatibility than Sr-CGs, highlighting the potential biomedical applications of $CaCO_3$-based biomineralized materials. The potential of Ca-CGs

to promote osteogenesis and biodegradability *in vivo* will be investigated further.

Author contributions

Yizhou Zhang designed the research and carried out the experiments, analysed the data and wrote the manuscript. Yiru Wang carried out the biocompatibility testing and AFM/KPFM. Zhengyi Zhang conducted CD spectra analysis and prepared figures. Zhe Wang and Changyu Shao suggested the research design. Matthias Hannig and Zihuai Zhou suggested the research design and assisted in revising the manuscript. Baiping Fu supervised the project and revised the manuscript. All authors reviewed and discussed the manuscript.

Conflicts of interest

The authors (B. Fu, Y. Zhang, Z. Zhou and Y. Wang) declared that they have applied for patents concerning the collagen scaffolds mineralized with carbonates and their application in China (no. ZL202310494884.X). The other authors declare no conflict of interest.

Acknowledgements

References

1 K. Grandfield, C. Micheletti, J. Deering, G. Arcuri, T. Tang and B. Langelier, *Acta Biomater.*, 2022, **148**, 44–60.

2 C. Y. Wang, K. Jiao, J. F. Yan, M. C. Wan, Q. Q. Wan, L. Breschi, J. H. Chen, F. R. Tay and L. N. Niu, *Prog. Mater. Sci.*, 2021, **116**, 100712.

3 B. M. Oosterlaken, M. P. Vena and G. de With, *Adv. Mater.*, 2021, **33**, e2004418.

4 H. Ping, H. Xie, Y. M. Wan, Z. X. Zhang, J. Zhang, M. Y. Xiang, J. J. Xie, H. Wang, W. M. Wang and Z. Y. Fu, *J. Mater. Chem. B*, 2016, **4**, 880–886.

5 W. J. Landis, F. H. Silver and J. W. Freeman, *J. Mater. Chem.*, 2006, **16**, 1495–1503.

6 Y. Liu, N. Li, Y. P. Qi, L. Dai, T. E. Bryan, J. Mao, D. H. Pashley and F. R. Tay, *Adv. Mater.*, 2011, **23**, 975–980.

7 J. Li, J. F. Yan, Q. Q. Wan, M. J. Shen, Y. X. Ma, J. T. Gu, P. Gao, X. Y. Tang, F. Yu, J. H. Chen, F. R. Tay, K. Jiao and L. N. Niu, *Acta Biomater.*, 2021, **125**, 112–125.

8 Z. Z. Han, D. Li, H. Zhao, H. X. Yan and P. Y. Li, *Minerals*, 2017, **7**, 95.

9 F. C. Meldrum, *Int. Mater. Rev.*, 2003, **48**, 187–224.

10 M. C. Wan, W. Qin, C. Lei, Q. H. Li, M. Meng, M. Fang, W. Song, J. H. Chen, F. R. Tay and L. N. Niu, *Bioact. Mater.*, 2021, **6**, 4255–4285.

11 E. M. Gerhard, W. Wang, C. Y. Li, J. S. Guo, I. T. Ozbolat, K. M. Rahn, A. D. Armstrong, J. F. Xia, G. Y. Qian and J. Yang, *Acta Biomater.*, 2017, **54**, 21–34.

12 Y. Politi, T. Arad, E. Klein, S. Weiner and L. Addadi, *Science*, 2004, **306**, 1161–1164.

13 M. J. Olszta, X. G. Cheng, S. S. Jee, R. Kumar, Y. Y. Kim, M. J. Kaufman, E. P. Douglas and L. B. Gower, *Mater. Sci. Eng., R*, 2007, **58**, 77–116.

14 A. D. Woldetsadik, S. K. Sharma, S. Khapli, R. Jagannathan and M. Magzoub, *ACS Biomater. Sci. Eng.*, 2017, **3**, 2457–2469.

15 W. Yang, C. X. Yao, Z. Y. Cui, D. D. Luo, I. S. Lee, J. M. Yao, C. Chen and X. D. Kong, *Int. J. Mol. Sci.*, 2016, **17**, 639.

16 M. J. Olszta, E. P. Douglas and L. B. Gower, *Calcif. Tissue Int.*, 2003, **72**, 583–591.

17 D. C. Bassett, B. Marelli, S. N. Nazhat and J. E. Barralet, *Adv. Funct. Mater.*, 2012, **22**, 3460–3469.

18 M. Wang, H. B. Deng, T. Jiang and Y. N. Wang, *Biomater. Adv.*, 2022, **135**, 112670.

19 L. Yu and M. Wei, *Int. J. Mol. Sci.*, 2021, **22**, 944.

20 F. Nudelman, K. Pieterse, A. George, P. H. Bomans, H. Friedrich, L. Brylka, P. J. Hilbers, G. de With and N. J. M. Sommerdijk, *Nat. Mater.*, 2010, **9**, 1004–1009.

21 T. Iwatsubo, K. Sumaru, T. Kanamori, T. Yamaguchi and T. Sinbo, *J. Appl. Polym. Sci.*, 2004, **91**, 3627–3634.

22 Y. Wang, N. Van Manh, H. R. Wang, X. Zhong, X. Zhang and C. Y. Li, *Int. J. Nanomed.*, 2016, **11**, 2053–2067.

23 Y. F. Xu, F. Nudelman, E. D. Eren, M. M. Wirix, B. Cantaert, W. H. Nijhuis, D. Hermida-Merino, G. Portale, P. H. Bomans, C. Ottmann, H. Friedrich, W. Bras, A. Akiva, J. R. O. Orgel, F. Meldrum and N. Sommerdijk, *Nat. Commun.*, 2020, **11**, 5068.

24 T. X. Wang, H. Cölfen and M. Antonietti, *J. Am. Chem. Soc.*, 2005, **127**, 3246–3247.

25 P. M. Smeets, K. R. Cho, R. E. Kempen, N. J. M. Sommerdijk and J. De Yoreo, *Nat. Mater.*, 2015, **14**, 394–399.

26 Z. H. Zhou, L. Q. Zhang, J. C. Li, Y. Shi, Z. F. Wu, H. Y. Zheng, Z. Wang, W. J. Zhao, H. H. Pan, Q. Wang, X. G. Jin, X. Zhang, R. K. Tang and B. P. Fu, *Nanoscale*, 2021, **13**, 953–967.

27 W. H. Wang and K. K. Yeung, *Bioact. Mater.*, 2017, **2**, 224–247.

28 C. G. Huang, J. L. Zhou, J. Rao, X. Y. Zhao, X. M. Tian, F. P. He and H. S. Shi, *Colloids Surf., B*, 2022, **218**, 112755.

29 C. Y. Shao, R. B. Zhao, S. Q. Jiang, S. S. Yao, Z. F. Wu, B. Jin, Y. L. Yang, H. H. Pan and R. K. Tang, *Adv. Mater.*, 2018, **30**, 1704876.

30 Z. Ye, Y. P. Qi, A. Q. Zhang, B. J. Karels and C. Aparicio, *ACS Macro Lett.*, 2023, **12**, 408–414.

31 J. Elango, J. Y. Zhang, B. Bao, K. Palaniyandi, S. J. Wang, W. H. Wu and J. S. Robinson, *Int. J. Biol. Macromol.*, 2016, **91**, 51–59.

32 J. Lü, E. Delamarche, L. Eng, R. Bennewitz, E. Meyer and H. J. Güntherodt, *Langmuir*, 1999, **15**, 8184–8188.

33 M. B. Gindele, K. K. Malaszuk, C. Peter and D. Gebauer, *Langmuir*, 2022, **38**, 14409–14421.

34 A. Tsortos and G. H. Nancollas, *J. Colloid Interface Sci.*, 2002, **250**, 159–167.

35 M. G. Willinger, J. Polleux, M. Antonietti, H. Cölfen, N. Pinna and N. Nassif, *CrystEngComm*, 2015, **17**, 3927–3935.

36 W. J. Jin, Y. L. Jin, P. Q. Duan, H. Y. Wu, L. Q. Zhang, Q. L. Du, H. H. Pan, R. K. Tang and C. Y. Shao, *J. Mater. Chem. B*, 2022, **10**, 5826–5834.

37 Z. Y. Zou, L. Bertinetti, Y. Politi, P. Fratzl and W. E. M. Habraken, *Small*, 2017, **13**, 1603100.

38 T. Riaz, R. Zeeshan, F. Zarif, K. Ilyas, N. Muhammad, S. Z. Safi, A. Rahim, S. A. A. Rizvi and I. U. Rehman, *Appl. Spectrosc. Rev.*, 2018, **53**, 703–746.

39 D. M. Sun and Q. S. Wu, *Chin. J. Chem.*, 2004, **22**, 1067–1069.

40 K. M. Sajesh, K. Kiran, S. V. Nair and R. Jayakumar, *Composites, Part B*, 2016, **99**, 445–452.

41 K. S. P. Karunadasa, C. H. Manoratne, H. M. T. G. A. Pitawala and R. M. G. Rajapakse, *J. Phys. Chem. Solids*, 2019, **134**, 21–28.

42 T. Tone and N. Koga, *ACS Omega*, 2021, **6**, 13904–13914.

43 P. Ptáček, E. Bartoníčková, J. Švec, T. Opravil, F. Šoukal and F. Frajkorová, *Ceram. Int.*, 2015, **41**, 115–126.

44 S. W. Lee, Y. J. Kim, Y. H. Lee, H. Guim and S. M. Han, *Mater. Des.*, 2016, **112**, 367–373.

45 N. B. Singh and N. P. Singh, *J. Therm. Anal. Calorim.*, 2007, **89**, 159–162.

46 H. Ping, W. Wagermaier, N. Horbelt, E. Scoppola, C. H. Li, P. Werner, Z. Y. Fu and P. Fratzl, *Science*, 2022, **376**, 188–192.

47 K. Sawada, *Pure Appl. Chem.*, 1997, **69**, 921–928.

48 R. W. Clark and J. M. Bonicamp, *J. Chem. Educ.*, 1998, **75**, 1182–1185.

49 H. H. Liu, M. L. Lin, X. Liu, Y. Zhang, Y. Y. Luo, Y. Y. Pang, H. T. Chen, D. W. Zhu, X. Zhong, S. Q. Ma, Y. H. Zhao, Q. Yang and X. Zhang, *Bioact. Mater.*, 2020, **5**, 844–858.

50 C. A. R. Jones, M. Cibula, J. C. Feng, E. A. Krnacik, D. H. Mclntyre, H. Levine and B. Sun, *Proc. Natl. Acad. Sci. U. S. A.*, 2015, **112**, E5117–E5122.

51 A. Hoppe, N. S. Güldal and A. R. Boccaccini, *Biomaterials*, 2011, **32**, 2757–2774.

52 K. Glenske, P. Donkiewicz, A. Köwitsch, N. Milosevic-Oljaca, P. Rider, S. Rofall, J. Franke, O. Jung, R. Smeets, R. Schnettler, S. Wenisch and M. Barbeck, *Int. J. Mol. Sci.*, 2018, **19**, 826.

53 Z. Saidak and P. J. Marie, *Pharmacol. Ther.*, 2012, **136**, 216–226.

54 A. Aimaiti, A. Maimaitiyiming, B. Y. Xu, K. Aji, C. Li and L. Cui, *Stem Cell Res. Ther.*, 2017, **8**, 282.

55 T. Machalowski, J. Idaszek, A. Chlanda, M. Heljak, A. Piasecki, W. Swieszkowski and T. Jesionowski, *Carbohydr. Polym.*, 2022, **275**, 118750.

56 X. C. Wu, K. Walsh, B. L. Hoff and G. Camci-Unal, *Bioengineering*, 2020, **7**, 132.

57 J. Wang, Q. Q. Liu, Z. X. Guo, H. H. Pan, Z. M. Liu and R. K. Tang, *ACS Biomater. Sci. Eng.*, 2023, **9**, 1757–1773.

58 L. N. Niu, W. Zhang, D. H. Pashley, L. Breschi, J. Mao, J. H. Chen and F. R. Tay, *Dent. Mater.*, 2014, **30**, 77–96.

59 Z. H. Zhou, J. C. Li, Z. Wang, H. L. Zhang, Y. R. Wang, D. N. Shen, Z. F. Wu, M. J. Shen, H. H. Pan, Q. Wang, R. K. Tang, M. Hannig and B. P. Fu, *Adv. Healthcare Mater.*, 2023, 2300100.

60 M. A. Bewernitz, D. Gebauer, J. Long, H. Cölfen and L. B. Gower, *Faraday Discuss.*, 2012, **159**, 291–312.

61 S. Joshi, S. Kalyanasundaram and V. Balasubramanian, *Appl. Spectrosc.*, 2013, **67**, 841–845.

62 M. Andonegi, K. de la Caba and P. Guerrero, *Food Hydrocolloids*, 2020, **100**, 105427.

63 M. Akita, T. Kono, K. Lloyd, T. Mitsui, K. Morioka and K. Adachi, *J. Food Biochem.*, 2019, **43**, e13013.

64 J. Wang, X. L. Pei, H. Y. Liu and D. Zhou, *Int. J. Biol. Macromol.*, 2018, **106**, 544–550.

65 K. G. Grønlien, M. E. Pedersen, K. W. Sanden, V. Høst, J. Karlsen and H. H. Tønnesen, *Sustainable Chem. Pharm.*, 2019, **13**, 100166.

66 A. Kandamchira, S. Selvam, N. Marimuthu, K. J. Sreeram and N. N. Fathima, *Mater. Sci. Eng., C*, 2013, **33**, 4985–4988.